Electronic Supplementary Material (ESI) for Energy & Environmental Science.
This journal is © The Royal Society of Chemistry 2020

Supplementary Information

for

Unveiling the Mechanisms of Lithium Dendrite Suppression by Cationic Polymer Film Induced Solid-Electrolyte Interphase Modification

Seung-Yong Lee,[a] Junyi Shangguan,[ab] Judith Alvarado,[c] Sophia Betzler,[a] Stephen J. Harris,[a] Marca M. Doeff[c] and Haimei Zheng[ab]*

[a]Materials Sciences Division, Lawrence Berkeley National Laboratory, Berkeley, CA, USA.

[b]Department of Material Science and Engineering, University of California, Berkeley, CA, USA.

[c]Energy Storage and Distributed Resources Division, Lawrence Berkeley National Laboratory, Berkeley, CA, USA.

Correspondence to: *E-mail: hmzheng@lbl.gov

This Supplementary Information file includes:

Captions for Videos S1 to S5

Supplementary Notes 1 to 7

Figures and Figure Captions S1 to S17

Tables S1 to S3

Other Supplementary Materials for this manuscript include the following:

Videos S1 to S5

Supplementary Video Legends

Video S1. *In-situ* TEM of lithium plating under Sn@SnO_2 nanostructure-assisted cationic polymer coating. The estimated cationic polymer area density is ~70 mg/m^2.

Video S2. *In-situ* TEM of lithium plating under the cationic polymer coating without the assistance of Sn@SnO_2 nanostructures. Individual video frames are aligned based on the electrode positions to correct sample shifts that have occurred during recording. Videos S2–S5 follow this same post-processing procedure.

Video S3. *In-situ* TEM of lithium plating without the polymer coating.

Video S4. *In-situ* TEM of lithium plating under Sn@SnO_2 nanostructure-assisted cationic polymer coating. The estimated cationic polymer area density is ~6 mg/m^2.

Video S5. *In-situ* TEM of lithium plating under Sn@SnO_2 nanostructure-assisted cationic polymer coating. The estimated cationic polymer area density is ~0.3 mg/m^2.

Supplementary Notes:

Supplementary Note 1. $Sn@SnO_2$ nanostructure-assisted PDDA coating on electrodes in a liquid TEM cell.

1.1. Necessity and effectiveness of $Sn@SnO_2$ nanostructure-assisted PDDA coating method

Drop-casting of the poly(diallyldimethylammonium chloride) (PDDA) polymer solution on the electrode is the simplest method to coat the electrode with the PDDA. To coat the electrodes with the PDDA polymer in an assembled liquid TEM cell, a droplet of polymer solution may be loaded into one of the reservoirs and it is then drawn into the cell by capillary force through the gap (~150 nm) between the top and bottom chips[1] (Fig. S2). However, since the entanglement of polymer chains may clog the thin gap in the cell, the measured polymer area density appears to be not linearly correlated with the total volume of the polymer solution loaded into the cell. In this method, the polymer film density cannot be estimated, thus it is hard to conduct systematic studies.

Using the PDDA polymer solution with $Sn@SnO_2$ nanostructures can solve this issue. The fixed ratio of PDDA to Sn in the solution enables the estimation of PDDA area density using the area density of $Sn@SnO_2$ nanostructures observed in the viewing window. In addition, the liquid flow paths are not easily clogged because most of the polymer chains adhere to the surface of $Sn@SnO_2$ nanostructures without severe entanglement. We anticipate that the effects of cationic polymer on the lithium growth remain even with a small polymer density. This is because the cationic property of PDDA can be enhanced on the surface of $Sn@SnO_2$ nanostructures, by removing the chlorine anions from the polymer but leaving cationic backbones due to the electrostatic force in solution,[2] as proved by STEM-EDS shown in Fig. S1j,k. The weight ratio of PDDA to Sn in the colloidal solution was determined to be 1.1:1 by STEM-EDS quantification and this value was used to estimate the PDDA area density in Table S1. It will be further explained in Supplementary Note 1.3.

1.2. Synthesis of $Sn@SnO_2$ nanostructure-assisted PDDA solution

Here, we provide more details on the synthesis of $Sn@SnO_2$ nanostructure-assisted PDDA solution described in the *Experimental* section. First, $SnCl_4$ solution was added into the PDDA+$NaBH_4$ solution. $NaBH_4$ is a well-known reducing agent[3], which can reduce $SnCl_4$ to Sn. PDDA+$NaBH_4$ solution is likely to exchange anions resulting in BH_4 anions linked to pyrrolidinium cations of the PDDA backbone and making NaCl salt dissolved in the solution[4]. BH_4 anions attached to the PDDA backbone reduce $SnCl_4$ to Sn as soon as the $SnCl_4$ solution is added into the PDDA+$NaBH_4$ solution. Thus, the PDDA cationic backbone adhered to the reduced Sn nanostructure (with a thin layer of SnO_2 formed on the Sn surface). BH_4 anions are removed from the solution as a gas during the $SnCl_4$ reduction reaction as below[5]:

$$BH_4^- \rightarrow {}^{1}\!/_{2}B_2H_6 + {}^{1}\!/_{2}H_2 + e^- \qquad \text{Equation (S1)}$$

Accordingly, the resulting nanostructure colloidal solution is composed of Sn cores, SnO_2 surface layers, and PDDA cationic backbones adhered to the surface of the nanostructures by an electrostatic attraction with the negative charge of the SnO_2 surface layer. Most of the chlorine anions contained in the original PDDA solution were exchanged with BH_4 anions and were removed during the centrifugation. This maximizes the cationic property of the PDDA polymer, which can manifest its cationic properties even at very low concentrations in the liquid TEM cells at the nanoscale. The Sn@SnO_2 nanostructure-assisted PDDA solution in ethanol was ultrasonicated as the final step after centrifugation for several times. This is to separate some of PDDA from the surface of the Sn@SnO_2 nanostructures and enable the PDDA coating at the area where the Sn@SnO_2 nanostructures are not located. This step does not affect the total amount of PDDA in the solution.

1.3. Identification of Sn@SnO_2 nanostructure-assisted PDDA

TEM images and STEM-EDS data of the Sn@SnO_2 nanostructures supporting PDDA are shown in Fig. S1. A low magnification TEM image in Fig. S1a shows that most of the nanostructures are nanowires, while there are some shorter and thicker ones close to nanoparticles. A high-resolution TEM (HRTEM) image and its fast-Fourier transformed patterns in Fig. S1b–d confirm the α-Sn core and thin SnO_2 shell nanostructure. The cationic polymer, PDDA, on the surface of the nanostructures is not distinguishable by HRTEM images, but it could be identified by STEM-EDS shown in Fig. S1e–k. The nanostructures are dispersed onto the copper TEM grid with carbon film supporting layers. As shown in the EDS elemental maps, nitrogen signals are distinct at the area corresponding to that of Sn@SnO_2 nanostructures. Nitrogen is present in the PDDA backbone as shown in the chemical structure in Fig. 1a. EDS spectra (Fig. S1k) also confirm that nitrogen peaks are detected from the sample. Given that we used the Cu TEM grid with a carbon film supporting layer (Fig. S1i) as the substrate for the STEM-EDS measurement, PDDA is the only source of nitrogen. Accordingly, the composition ratio of PDDA to Sn can be determined by the atomic ratio of N to Sn elements from EDS spectra. It was measured that the atomic fraction of N to Sn is equal to 1.0, which draws the weight ratio of PDDA to Sn to be 1.1:1. EDS chlorine map shows a coarse density of chlorine element and the EDS spectrum confirms there is almost no signal of chlorine ions at 2.621 keV (Kα line) because most chlorine anions were washed during the centrifugation as explained in the section above.

Supplementary Note 2. Discussions on the lithium grain size analysis

In addition to the polymer density in the coating, we found that variations in the electrolyte thickness can also change the grain size of lithium nanogranules. For example, gas pockets are observed in the electrochemical liquid cells and the sizes of lithium nanogranules are distinctly different in areas with or without the gas pockets. It is noted that the gas pockets separating the areas of thin and thick liquid electrolyte are distinguished by the image contrast: dark contrast indicates thick electrolyte and bright contrast shows thin electrolyte with the gas pockets (Fig. S5, Videos S2,S4,S5). The dark contrast results from the higher scattering cross-section of electrons in the electrolyte than the area with gas pockets. Smaller lithium nanogranules were observed in the area with thinner electrolyte. However, the lithium nanogranular growth mode does not change regardless of the electrolyte thickness variations (Fig. 3a,b and Fig. S5,S8,S9). Lithium grain size distribution measurements (Fig. 3c) were conducted in the uniform liquid electrolyte layer with thickness of about 150 nm, as defined by the thickness of the spacer in the liquid cell. Therefore, effects of the electrolyte thickness in our analysis of nanogranule sizes can be ruled out. In addition, Fig. 1d shows uniform sizes of lithium nanogranules at the electrode edge or on the 90 nm-thick Ti electrode. It demonstrates that the growth of lithium nanogranules was not confined by the thin gap of the liquid cell. The local variations of the $LiPF_6$ salt concentration might also have contributed to the Li grain size variations in the individual experiments. However, their contribution should be similar in different experiments.

Gas pockets are often observed in liquid cell experiments[6, 7]. In many cases, they are induced by electron beam dissociation of liquids during imaging. In our experiments, the gas pockets likely result from gases trapped inside the liquid cell during electrolyte loading procedure. Since the electrolyte loading was conducted inside an argon-filled glove box, the gas pockets can be argon gases and inert.

Supplementary Note 3. Sample preparation for STEM-EDS experiments

For the STEM-EDS characterization of the *in-situ* grown lithium nanogranules after the *in-situ* lithium growth, the liquid electrolyte was first polymerized under the electron beam with a low and steady dose rate (~1 $e^-/Å^2s$)[8]. The e-beam polymerized electrolyte protects the lithium nanogranules from being damaged during the sample handling. Then, the liquid TEM cell was carefully separated to perform the STEM-EDS experiments in order to achieve enhanced EDS signals. The top and bottom SiN membranes also remained after the cell separation, which make double protection layers for the lithium and SEI. The solidified electrolyte layer not only protects the lithium and SEI layers from being damaged physically and chemically, but also makes the better electron beam tolerance of the sample during the STEM analysis. Comparison between a low-dose TEM image of the lithium captured from the *in-situ* TEM video and STEM images obtained under the solidified electrolyte layer confirms the stability of lithium in the presence of the protection layers (Fig. S12). The STEM-EDS elemental maps of C, O, F, and P around the well-defined dark region (corresponding to Li nanogranule) illustrate that the lithium nanogranules are well-preserved without side reactions (Fig. 4a).

Supplementary Note 4. Discussions on the measured current and the applied potential during the *in-situ* TEM lithium growth

4.1. Interpretations of the current measured during the *in-situ* liquid cell TEM experiments.

Electric current was measured by an external potentiostat device while voltammetry was applied to the liquid TEM cells during the *in-situ* TEM experiments (see Fig. S11). However, the measured current varies up to two orders of magnitude (10^{-1} to 10^{1} μA) in different *in-situ* TEM experiments. A noisy current plot is often obtained when lithium growth is observed during the *in-situ* TEM experiments. This might result from the inhomogeneous redox reactions, as evidenced by *in-situ* optical microscopy of lithium growth with noisy voltage profiles acquired[9].

We found that there is an almost 3-fold difference in the measured current under the similar lithium growth rates from several samples (Fig. 2,S11a,S11c). This is likely due to the impact of surrounding environment since the whole system was not in a Faraday cage with proper grounding. For example, the measured current is easily changed as the electronics connected to the same power strip are turned on or off.

Assuming all of the measured current contributed to the lithium growth on the electrodes *uniformly*, the measured current corresponding to the *in-situ* TEM experiment shown in Fig. 1c (Fig. S11a; ~1 μA) and Fig. 1e (Fig. S11c; ~0.5 μA) can be transformed into a current density of ~1.4 mA/cm^2 and ~0.7 mA/cm^2. This is much smaller than the current densities (~15–20 mA/cm^2; Fig. 2) calculated based on the observed lithium growth rate at the edge of the electrodes. This confirms that the lithium growth reactions preferentially occurred at the electrode edge closest to the counter electrode because of a large local electric field.

4.2. Electrochemical reactions in a liquid TEM cell nanobattery vs. a coin cell battery

For the design of our electrochemical experiments using a liquid TEM cell, we first explored an appropriate range of potential for the experiments. We found that a high overpotential has been commonly observed in *in-situ* studies of lithium plating using nanoscale liquid cell devices[10-12]. For example, it was reported that a potential of about -4V was required to induce lithium plating in liquid TEM cells in voltammetric experiments[10]. Another report showed that a potential of about -3V was measured for lithium deposition in a three-electrode liquid TEM cell under galvanostatic mode[11]. The variations in the potential for lithium plating may arise from the different liquid cell design. In a different report, the counter electrode voltage approached 4 to 6V while the Li-depositing working electrode reached about -3V (vs. the reference electrode) under galvanostatic mode[12]. It suggested that the oxidative reaction at the counter electrode may have changed the potential. Therefore, we applied the potential in the range of 0 to -4V or 0 to -6V with a linear-sweep function (-100 mV/s) in our *in-situ* liquid cell TEM experiments. The wide range of the applied potential assists in capturing the lithium plating. The high potential and the high sweep rate also speed up the lithium electrodeposition reaction, minimizing the electron beam effect during the *in-situ* TEM experiments.

Our experiments show that lithium started to nucleate at a potential between -1V and -3V (see Videos S1–S5). We consider the observed overpotential for lithium plating likely arises from the thin liquid TEM cell devices. Previous studies showed that the measured viscosity of a thin liquid in a liquid TEM cell is much higher than that of the bulk liquid (up to six orders of magnitude)[13]. This suggests that the ionic diffusion in the thin liquid electrolyte can be significantly slower, thus a large voltage drop in the liquid TEM cell is expected. Argon gas pockets in the liquid TEM cell may have also made contribution in this aspect. Another factor that may have contributed to the observed overpotential includes oxidative reactions at the counter electrode, such as electrolyte decomposition.

We further evaluate the impacts of our high applied potential on lithium plating (e.g. 1 to 3V higher than that required for lithium plating in a liquid cell). Our series of experiments show that the applied potential does not lead to abnormal reactions in lithium plating. For instance, all the experiments show consistent lithium plating behavior as reported in the main text, irrespective of the shift in the potential for initiation of lithium plating (between -1V and -3V).

In conclusion, we expect that the lithium deposition in our *in-situ* liquid cell TEM experiments does not impose critical differences from the lithium plating reactions in coin cells.

Supplementary Note 5. Further discussions on the Li/Cu coin cell test results

Fig. S15 shows typical discharge profiles of Li/Cu cells[14]. Bare and the cationic polymer coated Cu foils were discharged at 10 mA/cm^2 to a capacity of 1 mAh/cm^2 in CR2032 coin-type Li/Cu cells. A high current density was applied for the coin cell tests in order to be comparable to that in the *in-situ* liquid cell TEM experiments (Fig. 2). The overpotential for nucleation and the reduced overpotential during the growth are observed in both profiles. The cationic polymer coated cell has a slightly higher overpotential as expected because of the resistance created by the polymer film.

The presence of a cationic polymer film is confirmed by XPS spectrum of N 1s peak at ~402.5 eV (Fig. S17). This peak originates from the nitrogen in the pyrrolidinium cations of PDDA. Nitrogen peaks at ~398 eV in both samples may be attributed to the Si/SiN substrate supporting the samples. It is hard to identify the contributions of each oxygen and lithium compound in the XPS spectra of O 1s and Li 1s because there is little binding energy difference for most oxygen and lithium compounds[15-17]. However, the positive shift of the Li 1s peak in the polymer-coated cell is consistent with the increment of LiF SEI amount considering the exceptionally high binding energies of lithium halides compared to other typical lithium SEI compounds[15, 16].

The low magnification SEM image in Fig. S16 shows the dominant nanogranular morphology of lithium under the cationic polymer film. Given that previous developments for lithium dendrite suppression mostly showed their effectiveness up to moderate current densities (~1–3 mA/cm^2)[18-21], it is surprising that the cationic polymer film showed effectiveness even at very high current densities. The lithium nanogranules are not perfectly uniform and there still are rod-type lithium grains in the polymer-coated cell; however, our results demonstrate the effectiveness of the cationic polymer for lithium dendrite suppression and provide a previously unexplored and unique mechanism for suppressing lithium dendrites. We expect that the cationic polymer film can be further improved, and more creative ways to maximize the advantage of the cationic polymer properties will be developed. As a side note, one should consider that the film effect can be confined to the surface close to the film. It should be further investigated how film thickness controls lithium growth as it is pushed away from the electrode during the lithium plating, irrespective of the species of the coating layer.

Supplementary Note 6. Investigations of electron beam effects on lithium nanogranular growth

For the *in-situ* TEM observations of lithium nucleation and growth, very low electron dose rate of ~0.2–0.5 $e^-/\text{Å}^2s$ was used, which is smaller than common electron dose rate, i.e. ~1 $e^-/\text{Å}^2s$, for previous liquid TEM studies.[7, 10, 22] Nevertheless, we further carefully examined if there was any influence of the electron beam on the nanogranular growth of lithium. For the investigation, the same experimental environment as for the Li nanogranular growth observation was created, except the electron beam irradiation. For example, a Li/Li symmetric liquid TEM cell with the Sn@SnO_2 nanostructure-assisted PDDA coating layer was loaded into the TEM column and the sweep-step function was applied through the holder in the TEM column. Lithium was plated for 240 s (linear sweep potential from 0 to 4 V at 0.1 V/s rate followed by constant potential bias at 4V for 200 s) without electron beam irradiation at this electrode. Fig. S6 shows the result of this control experiment. As shown in the TEM image, lithium nanogranules were grown without any dendritic structure, same as under the electron beam irradiation. This control experiment confirms that the nanogranular growth of lithium has not originated from the electron beam irradiation.

Supplementary Note 7. Sn@SnO_2 nanostructure effects on lithium nanogranular growth

To examine the influence of Sn@SnO_2 nanostructures upon Li nanogranular growth, we also performed the *in-situ* TEM observations of Li electrodeposition without the Sn@SnO_2 nanostructures. 0.05 wt% PDDA in ethanol solvent was dropped twice and dried overnight to coat the cationic polymer on the electrodes in an electrochemical liquid TEM cell. Since the entanglement of polymer chains may clog the thin gap in the cell, the polymer area density is not linearly correlated with the total volume of the polymer solution loaded into the cell. Therefore, the polymer film density cannot be estimated in this configuration. Nevertheless, the nanogranular growth of lithium was observed during our *in-situ* TEM observations as shown in Fig. S7 and Video S2. A TEM image obtained after the *in-situ* experiment clearly shows the Li nanogranules on the face and the side of the electrode without any dendrites. It tends to show smaller Li nanogranules on the face than the side of the electrode, which may be attributed to the easier nucleation on the face due to the larger surface area as nucleation sites. These two sets of the control experiments (Supplementary Notes 6 and 7) confirm that the nanogranular growth of lithium has entirely originated from the PDDA cationic polymer, not from the electron beam (Supplementary Note 6) or the Sn@SnO_2 nanostructures (Supplementary Note 7).

Supplementary Figures

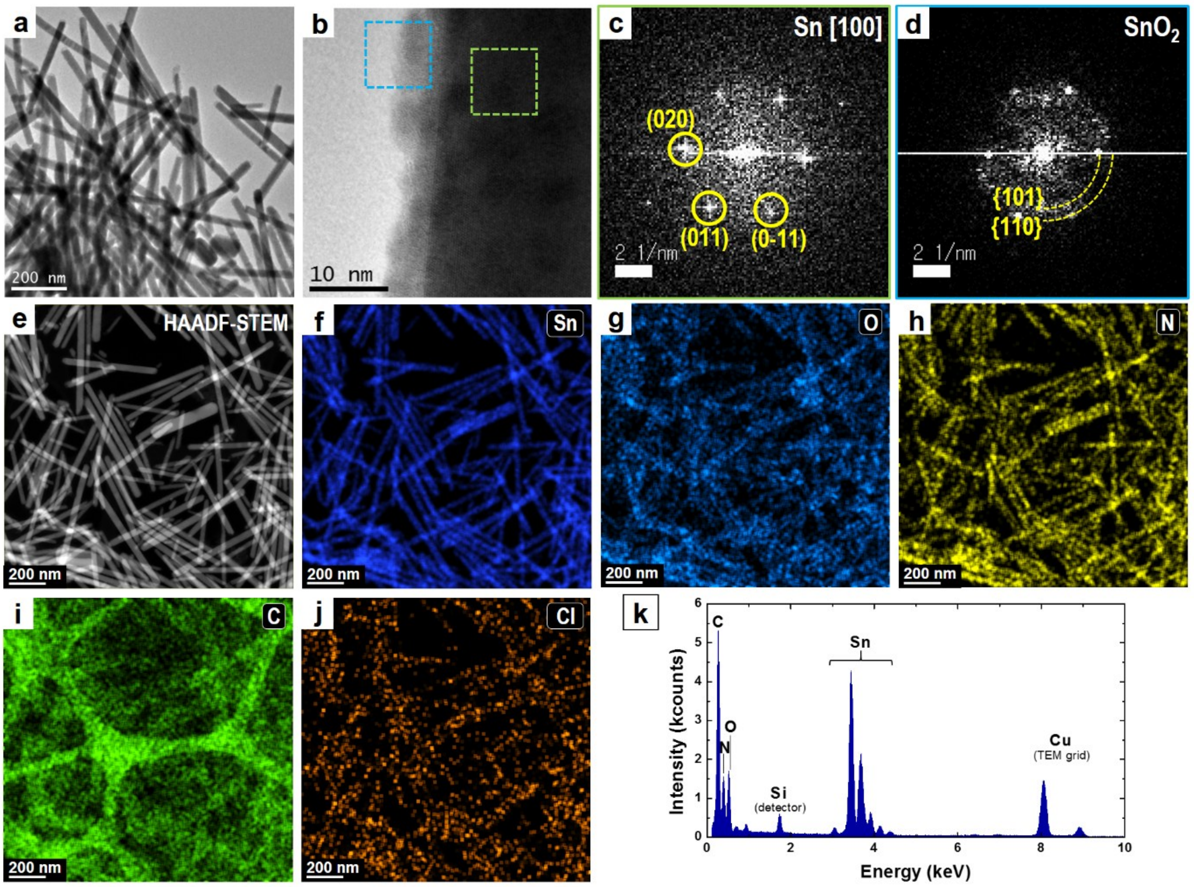

Fig. S1. Sn@SnO$_2$ nanostructures supporting PDDA polymer. (a) A low-magnification TEM image of Sn@SnO$_2$ nanostructures supporting PDDA. (b) A representative high-resolution TEM (HRTEM) image of a Sn@SnO$_2$ nanostructure. (c, d) Fast Fourier-transformed (FFT) patterns from (c) the inside and (d) the surface of the HRTEM image of the nanostructure marked in (b). (e–k) Scanning TEM energy-dispersive X-ray spectroscopy (STEM-EDS) analysis of the nanostructures. The nanostructures were dispersed onto a copper TEM grid with carbon film supporting layers. (e) A high-angle annular dark-field (HAADF) STEM image of nanostructures. (f–j) EDS elemental maps of (f) tin, (g) oxygen, (h) nitrogen, (i) carbon, and (j) chlorine in the area of the HAADF-STEM image shown in (e). (k) EDS spectrum acquired during the elemental mapping. See Supplementary Note 1 for further discussions.

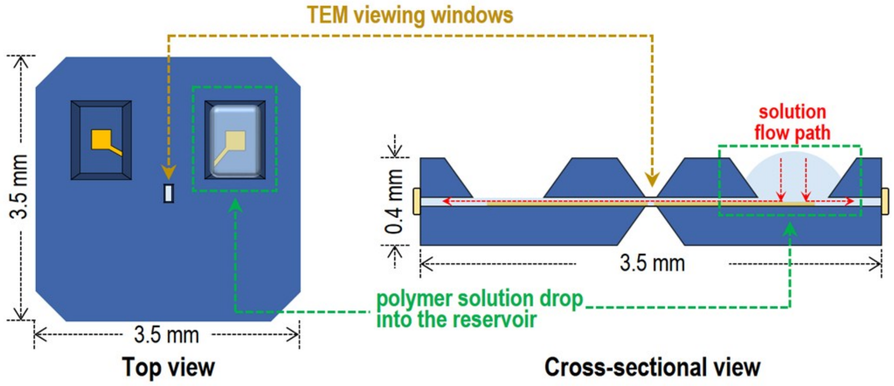

Fig. S2. Schematic drawings of top and cross-sectional views of an electrochemical liquid TEM cell and pre-coating the electrodes with PDDA polymer by drop-casting the polymer solution. The polymer solution has to flow through ~150 nm-thick gap between the cells to be coated onto the electrodes at the TEM viewing window.

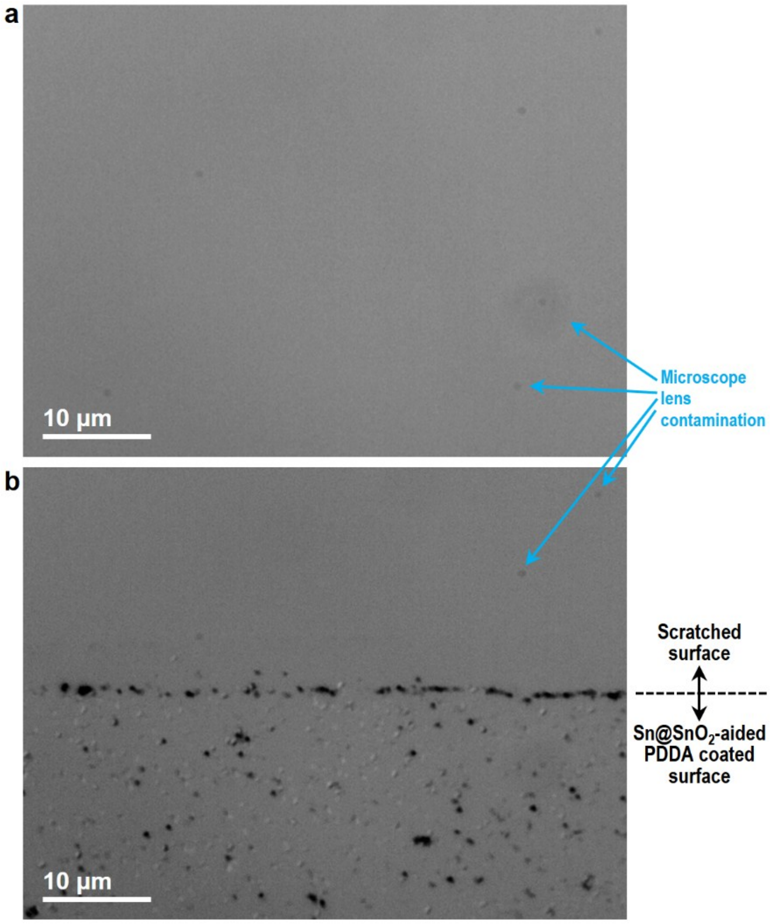

Fig. S3. Optical microscope images of Sn@SnO_2 nanostructure-assisted PDDA coated on electrochemical liquid TEM cells. Surface of bottom Si/SiN chips (a) without and (b) with Sn@SnO_2 nanostructure-assisted PDDA coating. For the coating, the Sn@SnO_2 nanostructure-assisted PDDA solution was loaded in the assembled electrochemical liquid TEM cell as described in Fig. S2. The cell was dried for a week and separated to acquire the optical microscope image. To create an area without the coating for comparison, certain area was scratched by a razor blade, which is clearly distinguished in the image in (b).

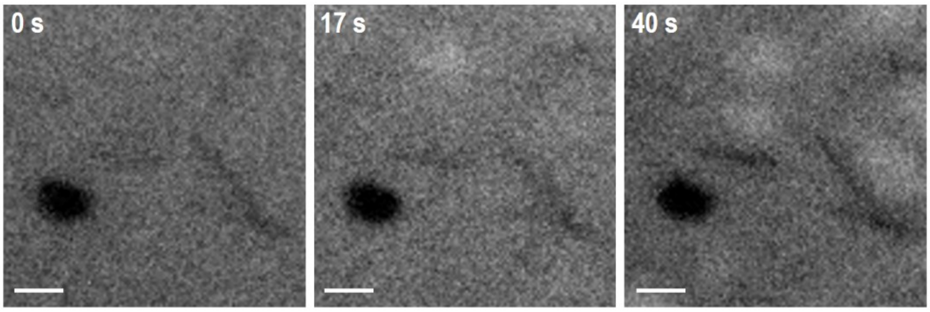

Fig. S4. Examination of contribution of Sn@SnO$_2$ nanostructures into redox reactions during *in-situ* TEM experiments. A series of TEM images captured during the *in-situ* TEM lithium plating experiments in the presence of Sn@SnO2 nanostructure-assisted PDDA coating. Nanomaterials with dark contrasts correspond to the Sn@SnO$_2$ nanoparticles/nanowires. Bright contrasts in the second and the third images correspond to the *in-situ* deposited lithium nanogranules. The TEM images show that the Sn@SnO$_2$ nanostructures are inactive without experiencing redox reactions during the *in-situ* lithium plating in the electrochemical liquid TEM cell. Scale bars are 200 nm.

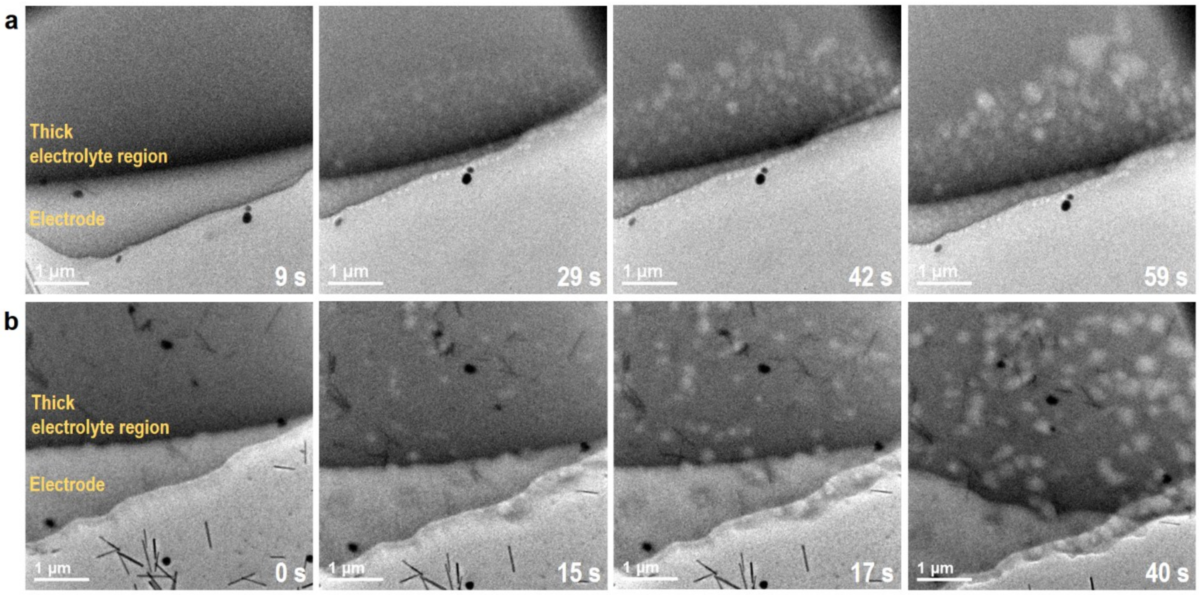

Fig. S5. *In-situ* TEM lithium growth with different area densities of the cationic polymer coating. Captured TEM images of the *in-situ* lithium plating under (a) the lowest (0.3 mg/m^2; Video S5) and (b) medium (5 mg/m^2; Video S4) area densities of the Sn@SnO$_2$ nanostructures, which correspond to the estimated polymer densities of ~0.3 mg/m^2 and ~6 mg/m^2. The highest concentrated one (nanostructure density of 60 mg/m^2; polymer density of ~70 mg/m^2) is shown in Fig. 1c (Video S1). Estimation of the PDDA density from the Sn@SnO$_2$ nanostructures is described in Supplementary Note 1. Elapsed time during the *in-situ* voltammetry experiment is written on individual images.

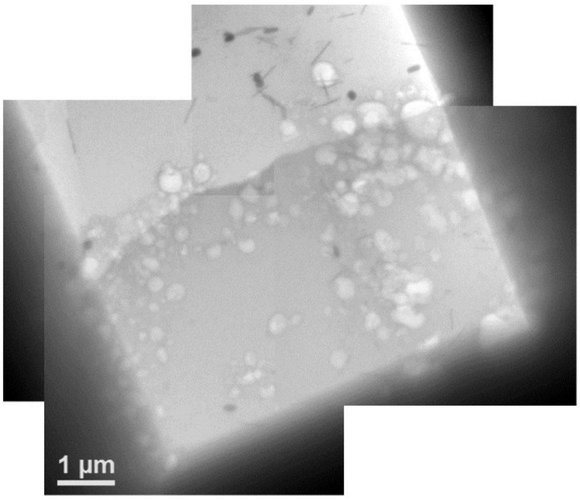

Fig. S6. Investigation of the electron beam effect on the growth of the lithium nanogranules. TEM images of lithium nanogranules grown in the TEM column under the cationic polymer coating as a voltammetric response, but without the electron beam irradiation. For the lithium plating, linear sweep voltammetry was applied from 0 to 4 V, followed by the constant potential at 4V for 200 s. It confirms that the lithium nanogranular growth is not influenced by the electron beam irradiation. See Supplementary Note 6 for further details.

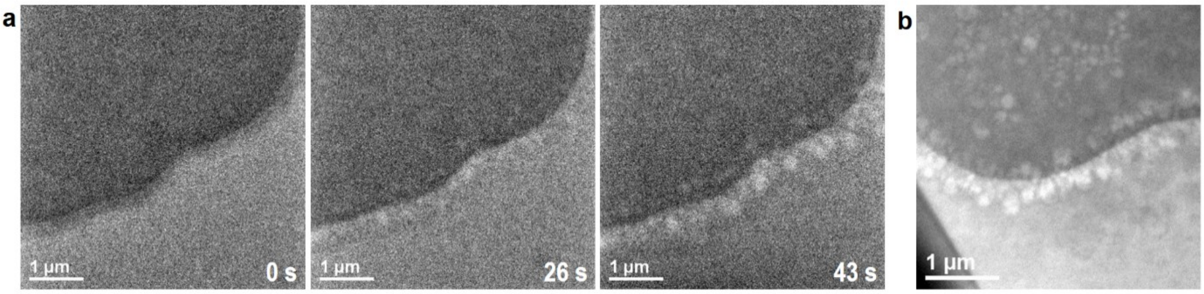

Fig. S7. An *in-situ* liquid cell TEM experiment with the cationic polymer coating but without the assistance of Sn@SnO$_2$ nanostructures. 0.05 wt% PDDA in ethanol solvent was dropped twice and dried overnight to coat the cationic polymer on the electrodes in an electrochemical liquid TEM cell. (a) Captured TEM images of the *in-situ* lithium metal plating with the PDDA coating without the assistance of Sn@SnO$_2$ nanostructures. Elapsed time during the *in-situ* voltammetry experiment is written on each image. (b) A TEM image of the *in-situ* grown lithium nanogranules acquired after the *in-situ* liquid cell TEM experiment. It confirms the same phenomena of the lithium dendrite suppression and the lithium nanogranular growth by the cationic polymer coating effect without the assistance of the Sn@SnO$_2$ nanostructures even though the density of the cationic polymer coating is not estimable. See Supplementary Note 7 for further details.

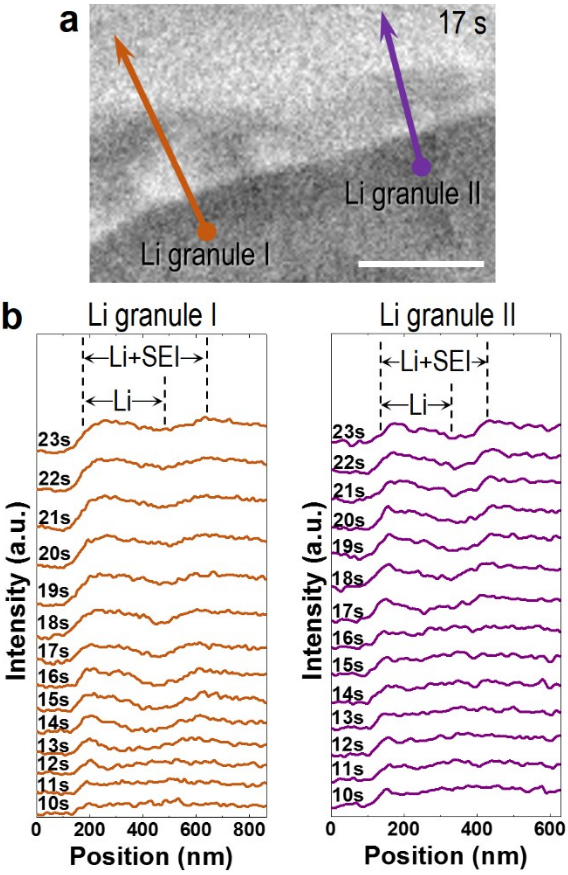

Fig. S8. Measurement details of individual lithium nanogranule and SEI sizes. (a) A captured TEM image marked with arrows indicating intensity line-scanning positions for the grain size analysis of lithium nanogranules I and II shown in Fig. 3b. The scale bar is 500 nm. (b) Line-scanned TEM intensity profiles for the size measurement of lithium nanogranules I and II and surrounding SEI layer. Intensity profiles are collected each second (10–23s) and stacked in a plot. The corresponding scanning lines are marked as arrows in (a). Position ranges of Li and Li+SEI at 23s are marked in each plot as examples.

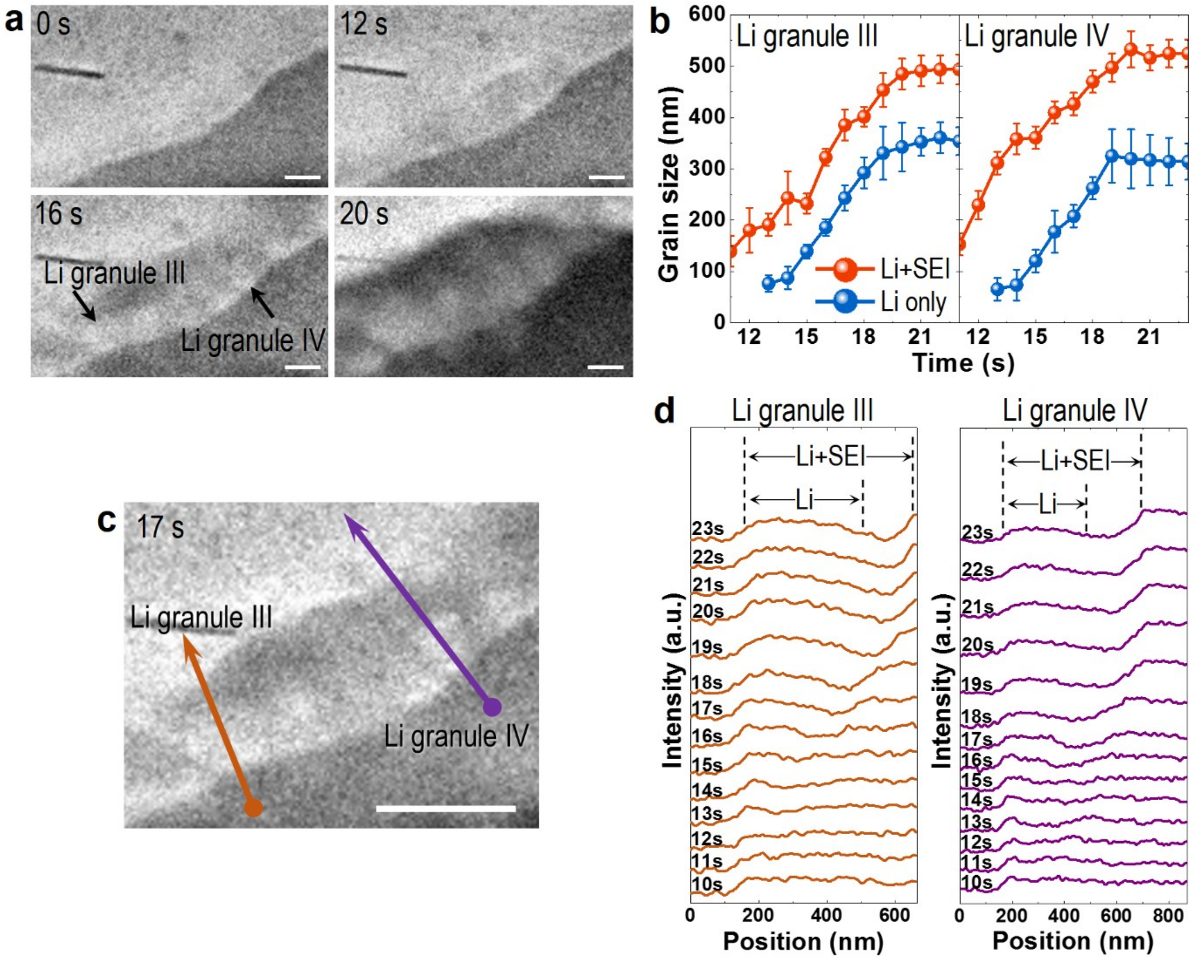

Fig. S9. Additional examples of *in-situ* lithium nanogranular growth showing the correlation between lithium and SEI layers. (a) Captured TEM images from an *in-situ* liquid cell TEM experiment of lithium and SEI growth. Scale bars are 200 nm. (b) Time vs. grain size plots of several lithium nanogranules and their SEI layers. Sizes of the lithium and the SEI formed after the potential application were measured. Round symbols and error bars indicate the average and minimum/maximum values of the grain sizes. Deposition of dark SEI layers is observed before lithium can be distinguished. (c) A captured TEM image marked with arrows, which indicate intensity line-scanning positions for the grain size analysis of lithium nanogranules III and IV shown in (b). The scale bar is 500 nm. (d) Line-scanned TEM intensity profiles of lithium nanogranules III and IV shown in (c). The corresponding scanning lines are marked as arrows in (c).

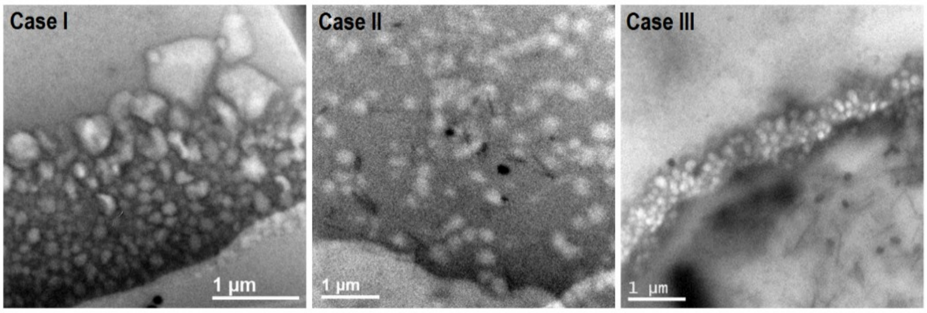

Fig. S10. Comparison of lithium nanogranular sizes depending on the density of the cationic polymer coating. TEM images of lithium nanogranules captured from a set of *in-situ* electrochemical liquid cell TEM experiments with different area density of the cationic polymer coating. The corresponding *in-situ* liquid cell TEM experiments are shown in Fig. S5 and Fig. 1c. Area densities of Sn@SnO_2 nanostructures and PDDA are estimated in Table S1.

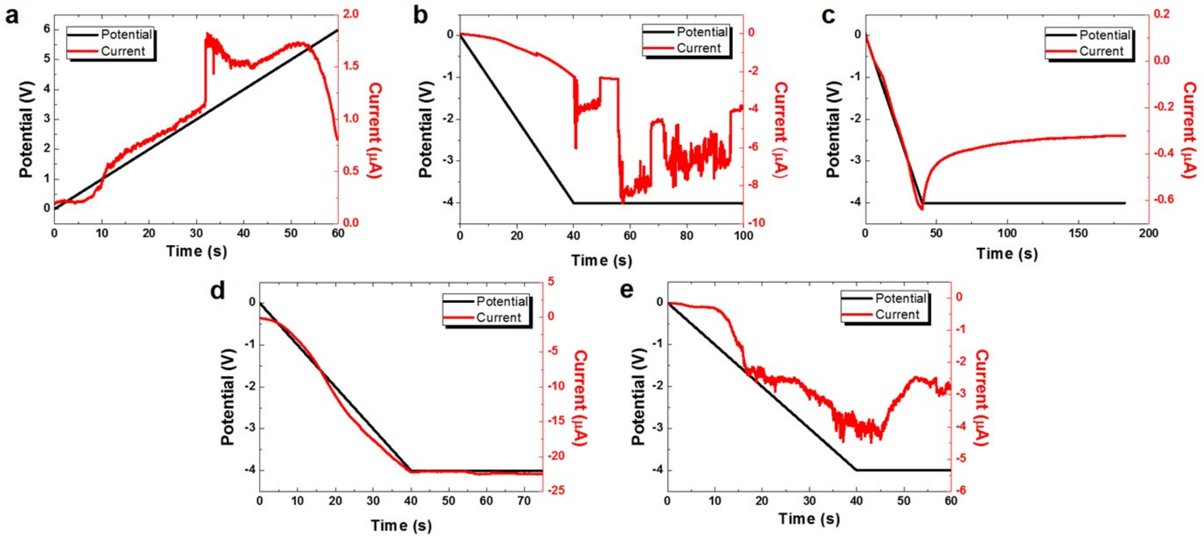

Fig. S11. Potential and current profiles as a function of time acquired during the *in-situ* liquid TEM experiments corresponding to (a) Video S1 and Fig. 1c, (b) Video S2 and Fig. S7, (c) Video S3 and Fig. 1e, (d) Video S4, Fig. 3a, and Fig. S5b, and (e) Video S5 and Fig. S5a. See Supplementary Note 4 for the further discussions.

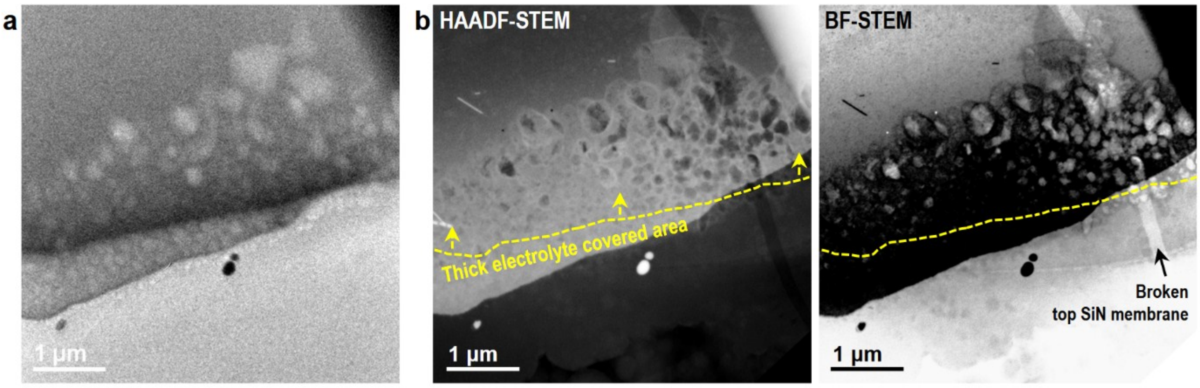

Fig. S12. Stability of the plated lithium metal under the protection layer of the solidified electrolyte. (a) A low-dose TEM image captured during the *in-situ* TEM voltammetry experiment. (b) HAADF and bright-field (BF) STEM images obtained after the formation of the solidified electrolyte protection layer on the plated lithium. Dark contrast in the HAADF STEM image and bright contrast in the BF STEM image show that most of the lithium nanogranules are well preserved under the converged electron beam of the STEM mode in the presence of the protection layer.

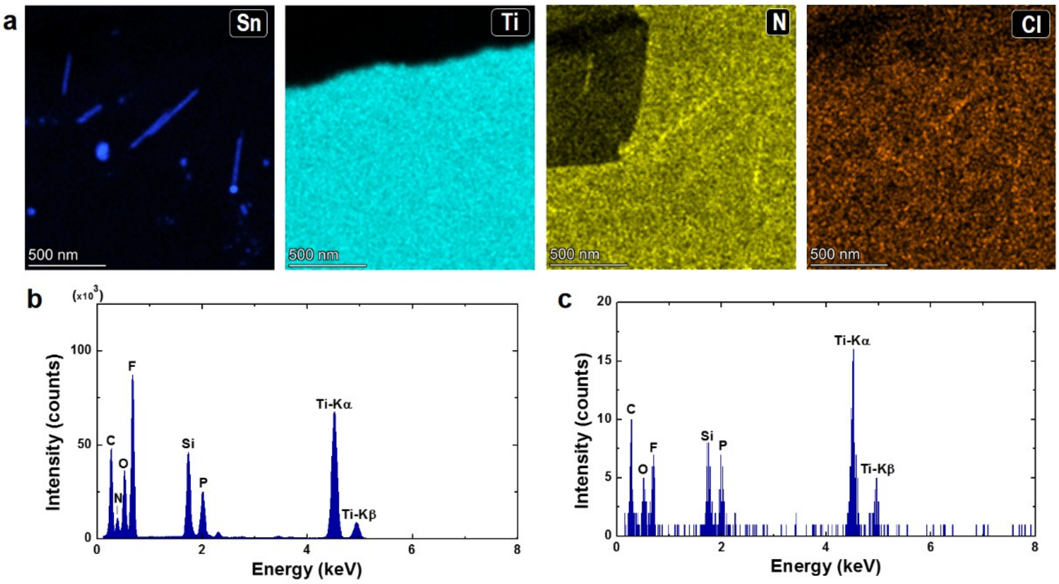

Fig. S13. Additional STEM-EDS data corresponding to the data shown in Fig. 4. (a) EDS elemental maps of tin, titanium, nitrogen, and chlorine at the area of the HAADF-STEM image shown in Fig. 4a. (b) EDS spectrum of the whole mapping area. (c) EDS spectrum of a representative single point for the line-scanning profile shown in Fig. 4c,d, which is integrated with a 100 pixels × 3 pixels window.

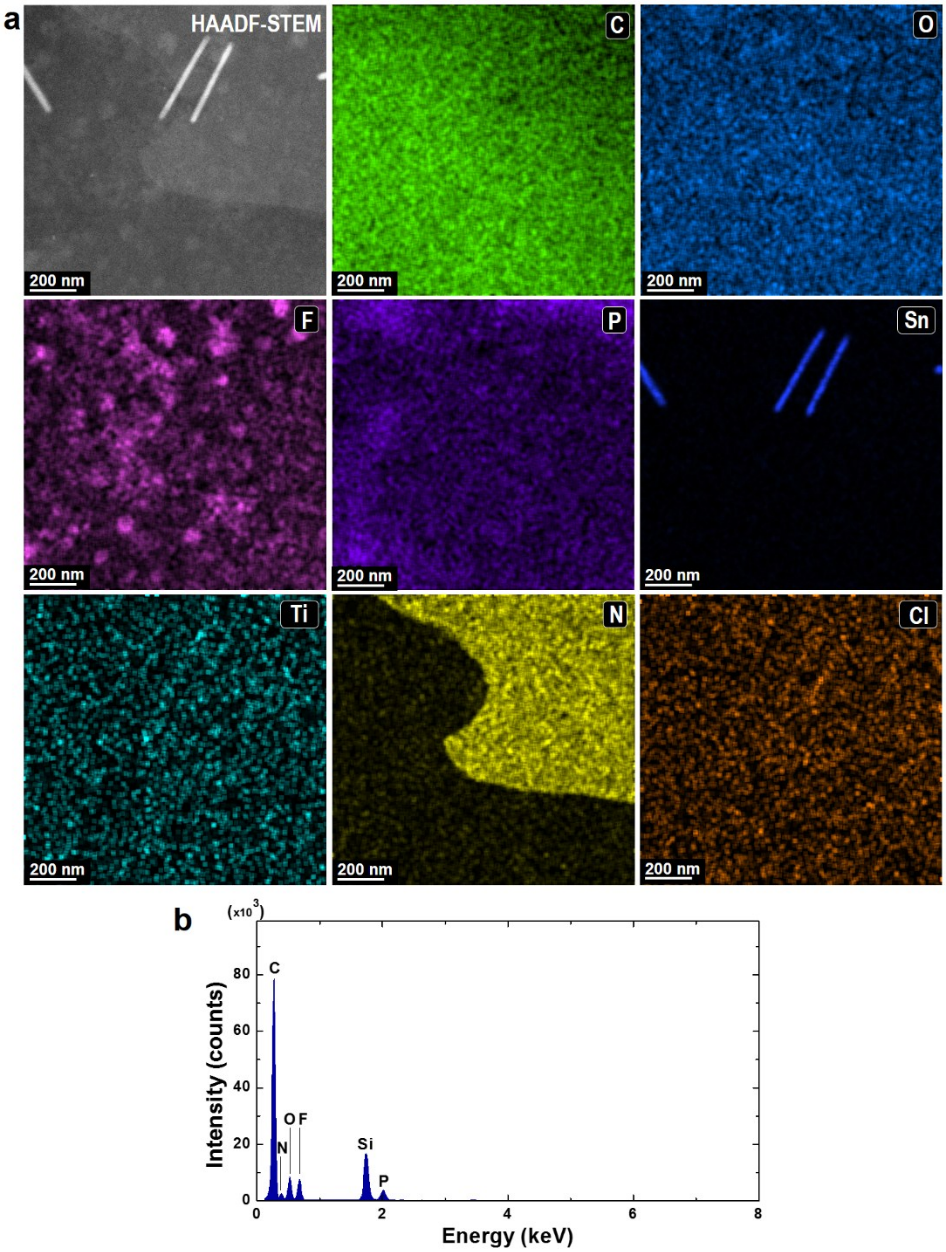

Fig. S14. STEM-EDS analysis of a region of electrolyte residue without lithium nanogranules and electrodes. (a) A HAADF-STEM image and EDS elemental maps of carbon, oxygen, fluorine, phosphorus, tin, titanium, nitrogen, and chlorine in the corresponding area. Distinctive shape in the nitrogen map originated from the stripped SiN membrane from the top chip of the electrochemical liquid TEM cell. (b) EDS spectrum obtained from the whole mapping area.

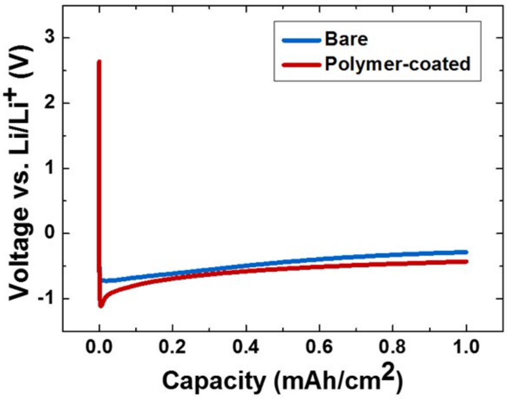

Fig. S15. Voltage profiles of Li/Cu cells discharged at 10 mA/cm^2 current density to a capacity of 1 mAh/cm^2 with and without the cationic polymer film, which are corresponding to the experiments shown in Fig. 5. See Supplementary Note 5 for further discussions.

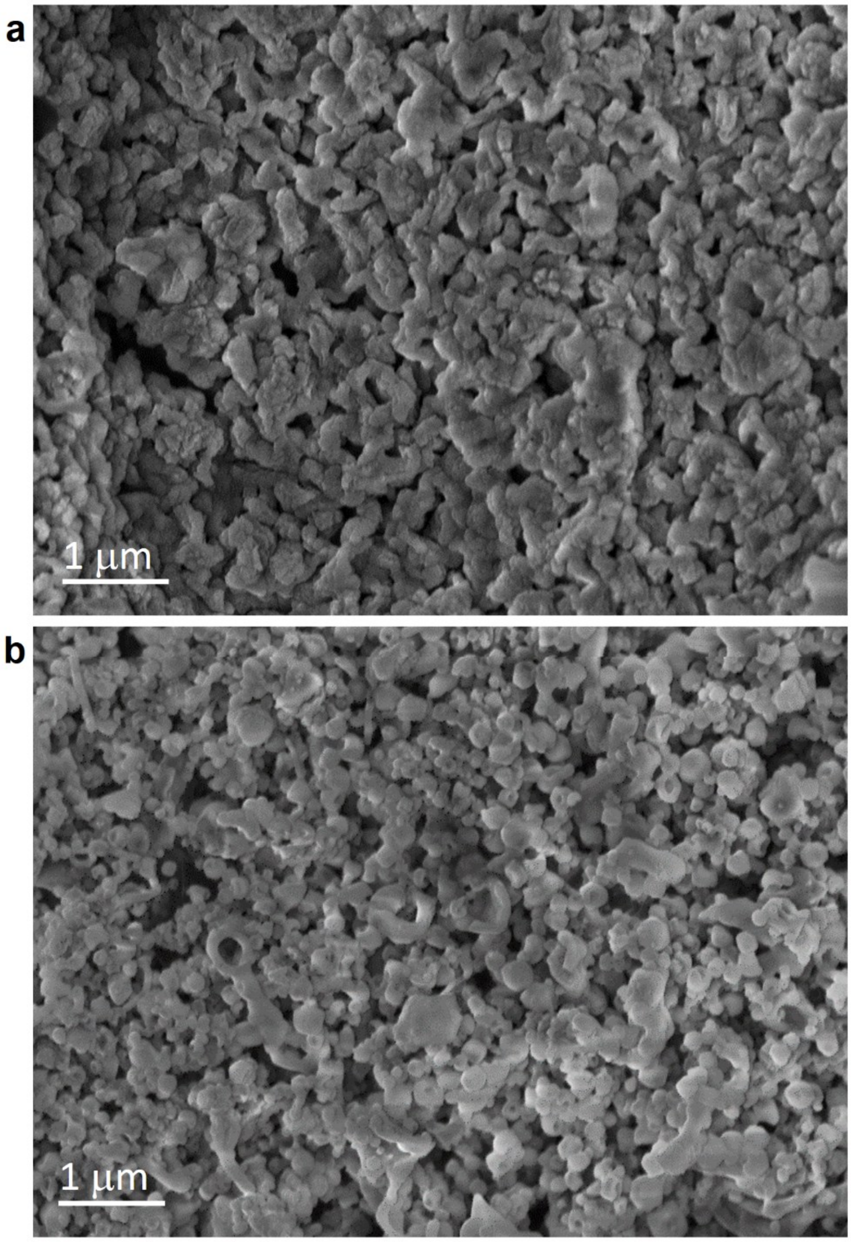

Fig. S16. Additional SEM images of lithium metal electrochemically plated in coin-type Li/Cu cells (a) without and (b) with the cationic polymer film, corresponding to Fig. 5a,b. See Supplementary Note 5 for further discussions.

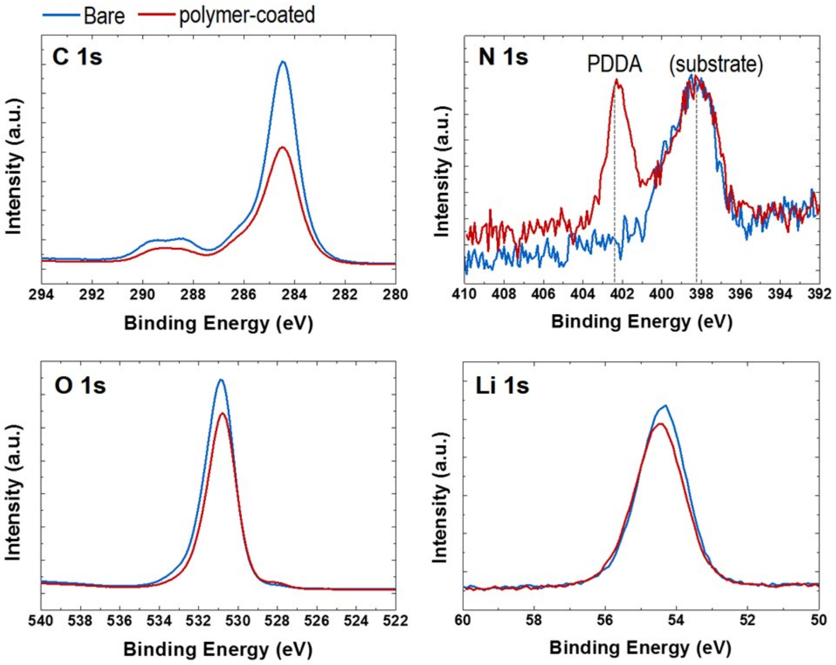

Fig. S17. Additional high-resolution XPS spectra of surface of lithium electrochemically plated in coin-type Li/Cu cells corresponding to Fig. 5c. See Supplementary Note 5 for the further discussions.

Table S1. Estimated area densities of Sn@SnO_2 nanostructures and PDDA on the electrode in each liquid TEM cell. Corresponding TEM images are shown in Fig. S10. The PDDA densities were estimated by STEM-EDS. The details are explained in Supplementary Note 1.

Experiment No.	Case I	Case II	Case III
Area density of Sn@SnO_2 nanostructures **(mg/m^2)**	3×10^{-1}	5	6×10^{1}
Estimated area density of PDDA **(mg/m^2)**	3×10^{-1}	6	7×10^{1}

Table S2. Atomic fractions of representative elements (C, O, F, and P) for SEI layers at the area concentrated with lithium nanogranules, shown in Fig. 4a and Fig. S13a. Atomic fractions are calculated based on the EDS spectrum of the whole mapping area shown in Fig. S13b.

Element	C	O	F	P
Atomic fraction	35 %	16 %	41 %	8 %

Table S3. Atomic fractions of representative elements (C, O, F, and P) for SEI layers at the area of electrolyte residue without lithium nanogranules, shown in Fig. S14a. Atomic fractions are calculated based on the EDS spectrum of the whole mapping area shown in Fig. S14b.

Element	C	O	F	P
Atomic fraction	89 %	5 %	4 %	2 %

References

1. Z. Y. Zeng, W. I. Liang, H. G. Liao, H. L. L. Xin, Y. H. Chu and H. M. Zheng, *Nano Lett*, 2014, **14**, 1745-1750.
2. K. Han, J. M. Shen, S. Q. Hao, H. Q. Ye, C. Wolverton, M. C. Kung and H. H. Kung, *Chemsuschem*, 2014, **7**, 2545-2553.
3. G. N. Glavee, K. J. Klabunde, C. M. Sorensen and G. C. Hadjapanayis, *Langmuir*, 1992, **8**, 771-773.
4. N. Du, H. Zhang, B. Chen, X. Ma and D. Yang, *Chem. Commun.*, 2008, 3028-3030.
5. T. Parnklang, B. Lamlua, H. Gatemala, C. Thammacharoen, S. Kuimalee, B. Lohwongwatana and S. Ekgasit, *Mater. Chem. Phys.*, 2015, **153**, 127-134.
6. J. M. Grogan, N. M. Schneider, F. M. Ross and H. H. Bau, *Nano Lett.*, 2014, **14**, 359-364.
7. A. Kushima, K. P. So, C. Su, P. Bai, N. Kuriyama, T. Maebashi, Y. Fujiwara, M. Z. Bazant and J. Li, *Nano Energy*, 2017, **32**, 271-279.
8. I. A. Shkrob, Y. Zhu, T. W. Marin and D. Abraham, *J. Phys. Chem. C*, 2013, **117**, 19270-19279.
9. P. Bai, J. Li, F. R. Brushett and M. Z. Bazant, *Energy Environ. Sci.*, 2016, **9**, 3221-3229.
10. B. L. Mehdi, J. Qian, E. Nasybulin, C. Park, D. A. Welch, R. Faller, H. Mehta, W. A. Henderson, W. Xu, C. M. Wang, J. E. Evans, J. Liu, J. G. Zhang, K. T. Mueller and N. D. Browning, *Nano Lett.*, 2015, **15**, 2168-2173.
11. K. L. Harrison, K. R. Zavadil, N. T. Hahn, X. B. Meng, J. W. Elam, A. Leenheer, J. G. Zhang and K. L. Jungjohann, *Acs Nano*, 2017, **11**, 11194-11205.
12. A. J. Leenheer, K. L. Jungjohann, K. R. Zavadil, J. P. Sullivan and C. T. Harris, *Acs Nano*, 2015, **9**, 4379-4389.
13. H. M. Zheng, S. A. Claridge, A. M. Minor, A. P. Alivisatos and U. Dahmen, *Nano Lett.*, 2009, **9**, 2460-2465.
14. R. Guo, L. G. Lu, M. G. Ouyang and X. N. Feng, *Sci. Rep.*, 2016, **6**, 30248.
15. C. S. Rustomji, Y. Yang, T. K. Kim, J. Mac, Y. J. Kim, E. Caldwell, H. Chung and S. Meng, *Science*, 2017, **356**, eaal4263.
16. X. Q. Zhang, X. Chen, X. B. Cheng, B. Q. Li, X. Shen, C. Yan, J. Q. Huang and Q. Zhang, *Angew. Chem. Int. Edit.*, 2018, **57**, 5301-5305.
17. N. Schulz, R. Hausbrand, C. Wittich, L. Dimesso and W. Jaegermann, *J. Electrochem. Soc.*, 2018, **165**, A833-A846.
18. Y. Y. Lu, Z. Y. Tu and L. A. Archer, *Nat. Mater.*, 2014, **13**, 961-969.
19. Y. Gao, Z. F. Yan, J. L. Gray, X. He, D. W. Wang, T. H. Chen, Q. Q. Huang, Y. G. C. Li, H. Y. Wang, S. H. Kim, T. E. Mallouk and D. H. Wang, *Nat. Mater.*, 2019, **18**, 384-389.
20. Y. P. Sun, Y. Zhao, J. W. Wang, J. N. Liang, C. H. Wang, Q. Sun, X. T. Lin, K. R. Adair, J. Luo, D. W. Wang, R. Y. Li, M. Cai, T. K. Sham and X. L. Sun, *Adv. Mater.*, 2019, **31**, 1806541.
21. B. Zhu, Y. Jin, X. Z. Hu, Q. H. Zheng, S. Zhang, Q. J. Wang and J. Zhu, *Adv. Mater.*, 2017, **29**, 1603755.
22. M. E. Holtz, Y. C. Yu, D. Gunceler, J. Gao, R. Sundararaman, K. A. Schwarz, T. A. Arias, H. D. Abruna and D. A. Muller, *Nano Lett.*, 2014, **14**, 1453-1459.